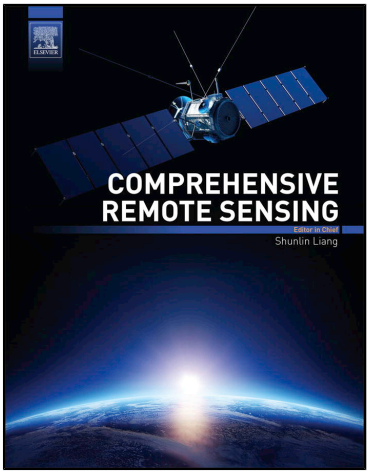

From Perissin, D. (2018) Geometric Processing: Active Sensor Modeling and Calibration (SAR). In S. Liang (Ed.), Comprehensive Remote Sensing, vol. 2, pp. 61–76. Oxford: Elsevier.
ISBN: 9780128032206

2.04 Geometric Processing: Active Sensor Modeling and Calibration (SAR)

D Perissin, Lyle School of Civil Engineering, Purdue University, West Lafayette, IN, United States

2.04.1 Introduction

Soon after the first experiments based on electromagnetic waves (late 19th century), scientists and engineers understood that an important application of transmitting and receiving signals through the air was the remote detection of targets. Moreover, thanks to the capability to penetrate fogs and clouds, during day and night, it was easy to see the advantages on this technology over optical signals. It took some time anyway to develop the first RAdio Detection And Ranging (RADAR) device (early 20th century).

RADARs played a key role during the Second World War, in particular in the Battle of Britain, allowing the British RAF to defeat the German Luftwaffe, thanks to the detection of aircraft through fog and clouds. The impact of this technology in defense applications pushed the research in the United States on this subject, leading to the invention of Synthetic Aperture Radar (SAR) in the 1950s (Carl A. Wiley is generally recognized as the inventor, even if independently the concept was being conceived also at the University of Illinois in the same years). SAR is the technology that allows the generation of high-resolution radar images from moving platforms. Initially developed for aircraft, it was mounted on a civilian satellite (the US Seasat mission) for the first time in 1978 (Allan, 1983). Unfortunately, the satellite kept operative for only 106 days.

The first SAR Interferograms for terrestrial application were produced in the 1980s (Goldstein et al., 1988), proving the high potential of the exploitation of the phase of radar signals for detecting very precise range variations. However, only after archives of SAR images became available, the technology was developed to the point of maturity. This initially happened in Europe (for civilian applications), thanks to the European Space Agency, which sent in orbit ERS-1 and 2 satellites in 1992 and 1995, respectively. Several groups at that time started focusing on InSAR algorithms development (to mention a few of them, DLR, Delft University, Polytechnic of Milan (Bamler and Hartl, 1998; Hanssen, 2001; Ferretti et al., 2001). Multitemporal InSAR processing algorithms are still being developed; however the technology is nowadays adopted as a reliable monitoring option in many fields (Massonnet and Feigl, 1998; Perissin, 2016).

This article approaches the Radar/SAR/InSAR subject in a simple way, paying attention to the geometric aspects of the technology. The theoretical discussion is limited to the basics needed for understanding the general framework and for grasping the importance of the phase of the radar signal, the key interpreting factor of the radar localization capability. A few examples taken from real data are also proposed to the reader. Data were processed with the software developed by the author (www.sarproz.com), and the interested reader can apply for a license to reproduce them. For more advanced treatment of the subject, the reader can refer to Curlander and McDonough (1991) and Ferretti et al. (2007).

The article is organized in five sections: (1) Radar (1D localization), (2) SAR (radar imaging in 2D), (3) InSAR (introducing the third dimension, but with technical limitations), (4) Multi-Baseline InSAR (MBInSAR) (the way to a proper 3D system), and the fifth paragraph concludes the chapter with a validation of the presented theory based on a real data processing case.

2.04.2 Radar Positioning

A radar is a device that transmits electromagnetic waves through an antenna, listening then for echoes reflected back by targets. Primitive radar systems were based on the transmission of energy pulses. The time Δt taken by the pulse to travel from the antenna to the target and back is used to estimate the distance R_0 between them (see Fig. 1). Assuming that the signal is traveling in vacuum (at the speed of light c), and considering the two-way path, the distance can be calculated as

$$R_0 = \frac{c\Delta t}{2} \tag{1}$$

The capacity to distinguish between two close targets is called range resolution and it can be considered as a first approximation of the precision with which the distance radar-target is estimated. The range resolution of primitive radars was given by the length τ of the transmitted pulse. This was a clear limitation, considering that, for reaching the energy needed to detect a target in the presence of noise, a short pulse (good range resolution) requires high power.

The solution to this problem came with the discovery of continuous-wave (CW) radars and with the adoption of modulated signals like chirps. A chirp is a waveform whose frequency changes as a function of time, sweeping a given bandwidth B around the carrier frequency f_c. The frequency content of such \wave is used to increase the resolution of the system by filtering accordingly the received signal (using a matched filter, conceptually similar to a cross-correlation between the transmitted signal and the received one). We can simplify the discussion by assuming that the final waveform $\gamma(t)$ recorded by the radar after filtering the received signal can be written as follows

$$\gamma(t) = e^{j2\pi f_c \Delta t}\,\mathrm{sinc}[B(t-\Delta t)] \tag{2}$$

Or expressing it as a function of the range coordinate r and using the wavelength λ and speed of light c

$$\gamma(r) = e^{j\frac{4\pi}{\lambda}R_0}\,\mathrm{sinc}\left[\frac{2B}{c}(r-R_0)\right] \tag{3}$$

The above equations say that the recorded signal is made of two terms. The term that usually captures most of the attention is a cardinal sine (A cardinal sine is defined as $\mathrm{sinc}(x) = \frac{\sin(\pi x)}{\pi x}$) (see Fig. 2), and it represents the real component of the signal. The cardinal sine is centered around the range R_0 of the target of interest, and the width of its main lobe leads to the range resolution ρ_{rg} of the system

$$\rho_{rg} = \frac{c}{2B} \tag{4}$$

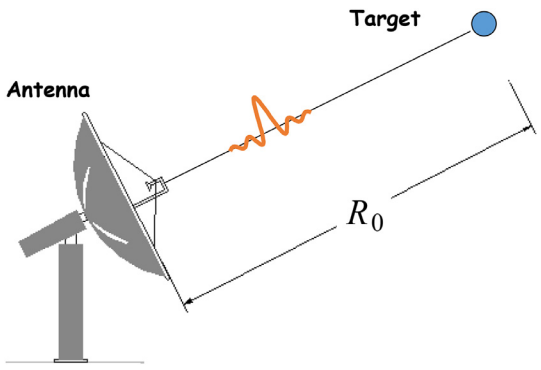

Fig. 1 Simplified sketch of a radar system. The antenna transmits a pulse; the pulse hits the target and travels back to the antenna. The radar measures the time between transmission and return of the pulse, and in this way it can retrieve the target range R.

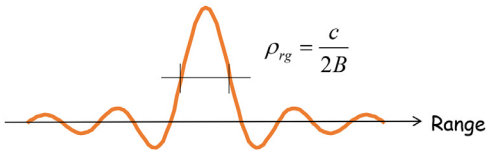

Fig. 2 The radar end-to-end system impulse response: the cardinal sine. The size of the main lobe of the cardinal sine corresponds to the resolution of the system and it is inversely proportional to the bandwidth B.

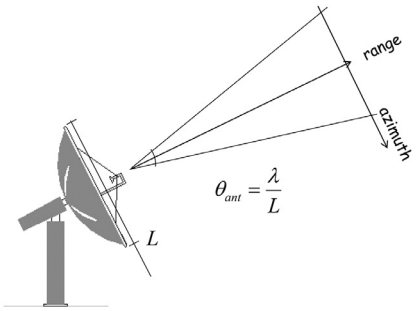

Fig. 3 Azimuth resolution of a radar system. The radar can detect only targets falling within the antenna beam. The aperture of the beam is equal to the wavelength divided by the antenna length.

The above equation shows that the resolution of the system is inversely proportional to the bandwidth B of the chirp (the higher the bandwidth, the better the resolution) and not directly related to its time duration. For systems, e.g., with 20 MHz bandwidth, the range resolution is about 7.5 m. This is the first element in our discussion that gives us (in first approximation) a quantification of the precision with which we can locate a target in range.

The left term in Eq. (3) is a complex exponential. For the sake of simplicity, we are neglecting other factors that are not useful for this discussion and we assume that its amplitude is equal to 1. The argument of the complex exponential is called phase ϕ, it corresponds to an angle and it is measured in radians

$$\phi = \frac{4\pi}{\lambda} R_0 \tag{5}$$

The left term in Eq. (3) it is often neglected. In fact the phase ϕ is still a function of the range R_0, but with a sensitivity equal to the wavelength λ, about three orders of magnitude smaller than the range resolution for common systems. The accuracy with which we can estimate the range R_0 from the peak of the cardinal sine (a fraction of the resolution cell in the best case) is not enough to read the phase of the complex exponential: the phase changes too fast as a function of R_0. Conversely, we cannot estimate R_0 from the phase of the complex exponential, because the phase is wrapped and ambiguous. We could thus conclude that the left term of Eq. (3) is not useful to better locate the target in space. Instead, we will see in the rest of this article that it is exactly that this term is the key to improve the localization ability of radar systems.

Simple radar systems cannot tell much about the position of a target in the direction orthogonal to the range. Since the antenna is directional and characterized by an angular aperture θ_{ant} (the signal propagates within the main lobe of the antenna scattering pattern), if a target is detected, we can simply conclude that its azimuth location falls within the antenna cone (see **Fig. 3**). The angular aperture θ_{ant} is a function of wavelength λ and antenna's length L

$$\theta_{ant} = \frac{\lambda}{L} \tag{6}$$

And, as a consequence, we can quantify the range-dependent radar azimuth resolution

$$\rho_{az} = \frac{\lambda}{L} R_0 \tag{7}$$

It is evident to realize that, with such a system, it would be particularly difficult to generate radar images: the azimuth resolution degrades linearly with the range distance. A radar mounted on a satellite at 800 km distance from the ground, with 10 m antenna and 5 cm wavelength, would have 4 km azimuth resolution.

2.04.3 Synthetic Aperture Radar Positioning

2.04.3.1 The SAR Impulse Response

To overcome the limited azimuth resolution, in the 1950s engineers discovered that, by mounting a radar on a moving device (as aircraft, spacecraft, or ground vehicles) and by analyzing coherently radar echoes from the same target from different sensor positions, it is possible to drastically increase the azimuth resolution of the system. This technology is called SAR, from the fact that the final azimuth resolution is corresponding to the one of a large "synthetic" antenna, built by combining the locations along the device trajectory from which a target is visible.

The SAR azimuth resolution improvement is ultimately possible, thanks to the complex term in Eq. (3). In fact, as we derive hereafter, the range variation along the sensor path is not big enough to be detected from the peak of the cardinal sine (the real term in Eq. 3). Instead, it can be detected by the phase of the complex term.

We define the Cartesian coordinate system x, y in **Fig. 4**. Sketch of the SAR acquisition system, where the sensor moves along the x–axis (left). The antenna illuminates the ground and its footprint at range R_0 equal to Δx. Set of positions from which the sensor

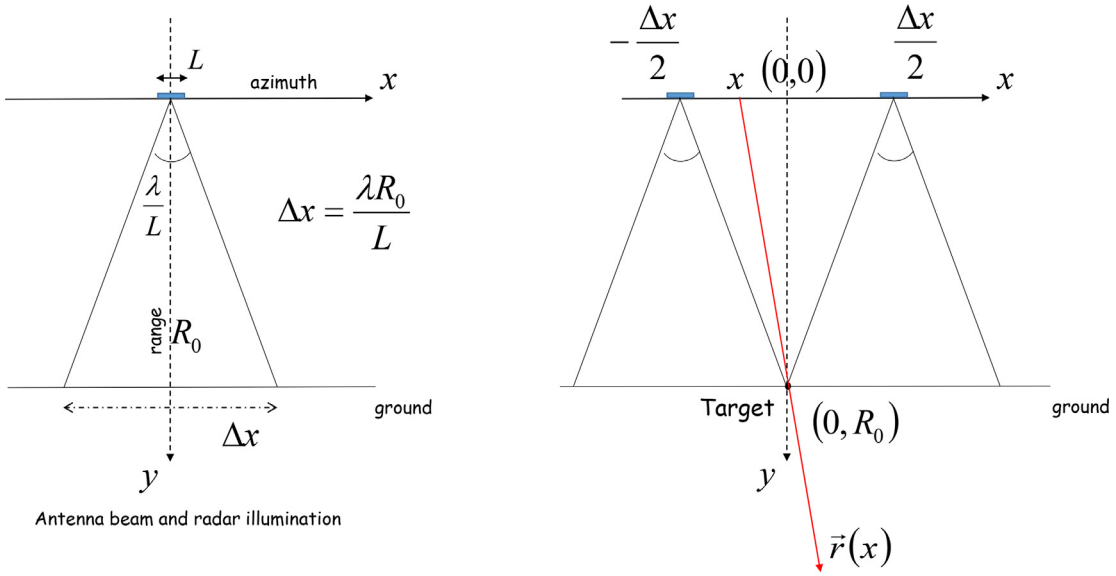

Fig. 4 Sketch of the SAR acquisition system. *Left*: the sensor moves along the *x*-axis. The antenna illuminates the ground and its footprint at range R_0 is equal to Δx. *Right*: set of positions from which the sensor illuminates the target located at $0, R_0$.

illuminates the target located at $0, R_0$ (right), with the sensor moving along the linear trajectory $x, 0$. The radar antenna is parallel to the trajectory and pointed towards the ground with looking direction orthogonal to it. A target is located on the ground at coordinates $0, R_0$. The range distance $R(x)$ between sensor and target as a function of the x coordinate is

$$R(x) = \sqrt{x^2 + {R_0}^2} \approx \frac{x^2}{2R_0} + R_0 \tag{8}$$

If we consider that the target must lie in the antenna beam in order to be visible by the radar, we obtain that Eq. (8) holds for a limited segment Δx of the sensor trajectory. The segment Δx corresponds to the radar illuminating footprint at range R_0

$$\Delta x = \frac{\lambda R_0}{L} \tag{9}$$

Given Eqs. (8) and (9) we can easily derive the maximum variation of $R(x)$ from R_0. Using the numbers given in the previous section, we obtain that the maximum range variation is about 2.5 m. If we consider that the range resolution ρ_{rg} is about 7.5 m, we can conclude that $R(x)$ will be hardly estimated from the peak of the cardinal sine. The phase of the complex term of Eq. (3) instead is much more sensitive to range variations. Even a small fraction of the wavelength (equal to 5 cm in our example) can be detected from the phase.

It could be at this point shown that the phase history $\phi(x)$ detected from the complex exponential in Eq. (3) and function of the azimuth coordinate x can univocally identify the azimuth location of the target.

$$\phi(x) = \frac{4\pi}{\lambda} R_0(x) \tag{10}$$

The condition to meet in order to correctly reconstruct the phase history $\phi(x)$, is to sample the x coordinate at a rate high enough to avoid aliasing of the phase. This condition determines the radar pulse transmission rate (Pulse Repetition Frequency, PRF).

From Eq. (8) we can recognize that the phase $\phi(x)$ is quadratic with x. The complex exponential $e^{\phi(x)}$ takes then the form of a modulated signal in azimuth (a chirp). The instantaneous frequency of the chirp can be calculated as

$$f(x) = \frac{2x}{\lambda R_0} \tag{11}$$

The bandwidth of the chirp B_{az} can be derived from the range of scanned frequencies, limited by the condition in Eq. (9)

$$B_{az} = \frac{2}{L} \tag{12}$$

Similarly to what happens in the range dimension, we can filter the received signal in the azimuth domain with a proper waveform and obtain a focused response in the form of a cardinal sine. The final range-azimuth SAR system response is then

$$y(r,x) = e^{j\frac{4\pi}{\lambda}R_0} \operatorname{sinc}\left[\frac{2B}{c}(r - R_0)\right] \operatorname{sinc}\left[\frac{2}{L}(x - X_0)\right] \tag{13}$$

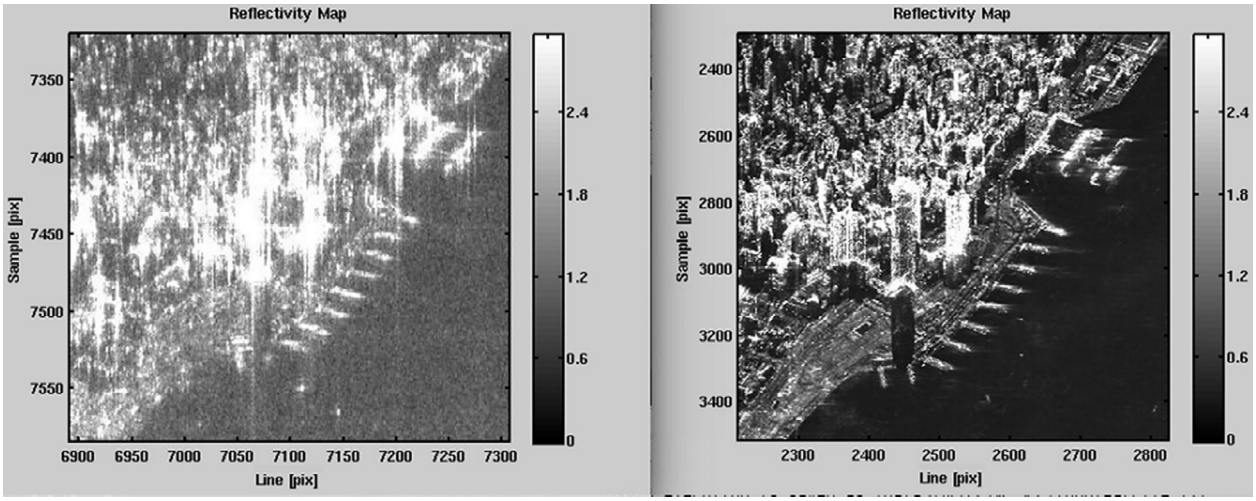

Fig. 5 SAR images over the Hong Kong harbor. *Left*: ALOS (L-band) image, *right*: TerraSAR (X-band). The two bands have different resolution and highlight different levels of details.

In Eq. (13), X_0 identifies the azimuth location of the target (assumed zero in Fig. 4 for the sake of simplicity).

The remarkable outcome of the SAR system is reaching an azimuth resolution equal to half the antenna length, thanks to the sensitivity of the phase. The smaller the antenna, the better the resolution. This apparent contradiction is explained by the fact that the smaller is the antenna, the longer is the section of the sensor trajectory from which the target is visible. Such a section behaves as a bigger apparent antenna, and it is called "synthetic aperture". Power budget conditions limit the minimum size of the antenna to be effectively used by SAR systems. In the example here, the antenna length is equal to 10 m, leading to an azimuth resolution of 5 m. Fig. 5 shows two examples of SAR images over the same area in Hong Kong. The image on the left was acquired by the ALOS satellite (L-band), while the one on the right was taken by TerraSAR-X (in X band).

2.04.3.2 From SAR to Ground Coordinates

The SAR technology is thus able to generate high-resolution radar images from long distance, allowing equipping aircraft and also spacecrafts with effective microwave imaging sensors. SAR images are complex matrixes organized in lines and samples. Lines correspond to the azimuth coordinate, samples to the range one. The sampling rate in both range and azimuth is chosen slightly higher than the respective bandwidth, so that multiple pixels will fall in the main lobes of the cardinal sines in Eq. (13). This situation guarantees that the complex information contained in the system response is preserved.

It is our aim now to geo-locate targets detected by SAR images. In addition to the radar equation (Eq. 3) leading to the range R_0, in SAR images we have a condition also on the azimuth coordinate X_0 (see Eq. 13). In our simplified discussion, the azimuth constraint corresponds to identifying the location from which the sensor observes the target at the shortest distance, that is, when the line connecting the sensor to the target is orthogonal to the platform trajectory. This condition corresponds also to constraining the time τ_0 in which the satellite is closer to the target.

Taking Fig. 6 as reference, we can find the relationship between SAR coordinates of a target P_0 (sample s and line l), its range R_0 and its acquisition time τ_0

$$R_0 = R_{offs} + s\frac{c}{2f_s} \tag{14}$$

$$\tau_0 = \tau_{offs} + l\frac{1}{PRF} \tag{15}$$

In Eqs. (14) and (15) R_{offs} and τ_{offs} are range and acquisition time of the first pixel of the SAR image. Pixel spacing is a function of range sampling frequency f_s and pulse repetition frequency PRF.

We can describe the sensor location and trajectory with position and velocity vectors (P_s and V_s, respectively) in a Cartesian coordinate system x,y,z (see Fig. 7). Position and velocity are a function of time τ. In the following, we exploit Eq. (15) to constrain satellite position and velocity to the time τ_0 when the satellite observes point P_0.

$$P_s = P_s(\tau_0) = [x_s \quad y_s \quad z_s]; \; V_s = V_s(\tau_0) = [v_{x,s} \quad v_{y,s} \quad v_{z,s}] \tag{16}$$

In the same system, we can define the target coordinates:

$$P_0 = [x_0 \quad y_0 \quad z_0]$$

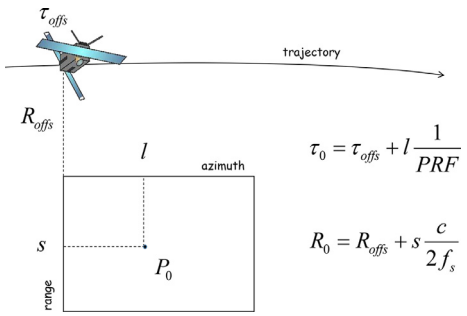

Fig. 6 SAR image coordinates (samples and lines) versus range and acquisition time.

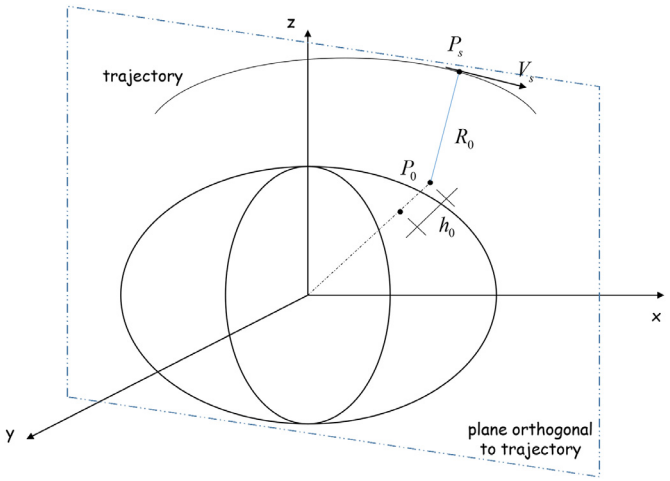

Fig. 7 Relationship between sensor and target coordinates in a Cartesian system. The sensor moves along the satellite trajectory and it observes target P_0 from position P_s. Both sensor and target belong to a plane orthogonal to the trajectory. The distance between target and sensor is the range R_0. The target is located at elevation h_0 with respect to a reference ellipsoid.

Range and azimuth equations can thus be expressed as follows

$$\sqrt{(x_s - x_0)^2 + (y_s - y_0)^2 + (z_s - z_0)^2} = R_0 \tag{17}$$

$$(x_s - x_0)v_{x,s} + (y_s - y_0)v_{y,s} + (z_s - z_0)v_{z,s} = 0 \tag{18}$$

The SAR equations are constraining two of the three needed coordinates to locate a target in the x, y, z space. The third condition must be sought somewhere else. In Earth Observation applications, targets are located on the Earth surface. By giving the Earth surface a mathematical form, we can then add a condition on the target coordinates P_0. We can, e.g., use the equation of the ellipsoid (described by semimajor and semiminor axes a and b), inflated by a factor h_0 corresponding to the target ellipsoidal height.

$$\frac{{x_0}^2 + {y_0}^2}{a^2\left(1 + \frac{h_0}{a}\right)^2} + \frac{{z_0}^2}{b^2\left(1 + \frac{h_0}{a}\right)^2} = 1 \tag{19}$$

Eqs. (17)–(19) constitute the system for the geolocation of targets detected in SAR images.

The first important consideration relates to the need for an external input: since SAR is a 2D system, the third condition for solving the system must be taken from an external DEM. Any problems related to the DEM will thus affect the correct geolocation of targets. Moreover, whenever the target is located above (or below) the surface described by the DEM, its final geolocation will be reflecting not its true position but its projection onto the DEM.

Beside the fact that a correct geolocation is external DEM-dependent, from Eqs. (17) and (18) we can also easily notice that the outcome is conditioned by orbit's accuracy. If the coefficients describing the platform trajectory are not accurate, the final target geolocation will be biased. Orbital accuracy is dependent on the adopted sensor. Moreover, different levels of accuracy are available depending on the orbital processing level (fast delivered orbits are less precise than postprocessed ones). We can anyway indicatively state that the orbital coefficients generally lead to a submeter accuracy in satellite positioning.

Orbital coefficients provide thus a precision higher than the SAR resolution. However, often range and timing offset in Eqs. (14) and (15) determine a rigid shift of the SAR image along the orbital trajectory. When this happens, the image will be geolocated in

a wrong position. This problem can be easily solved by correcting the initial offsets, with the help of Ground Control Points or, in the presence of topography, by simulating the ground reflectivity with an external DEM.

Given what we have discussed so far we can state that it is still improper to talk about SAR geolocalization. If we simply consider SAR as an imaging mode, then we have to treat it as a 2D technology, similar to the optical one. We can thus geocode a SAR image (project it to the ground), but we cannot estimate 3D coordinates of SAR targets.

To improve the localization of SAR targets, we may combine multiple SAR images taken with different viewing angles exploiting techniques such as stereo-photogrammetry (photogrammetric techniques translated in the SAR domain take the name of "radargrammetry"). Instead, in the next section we are still focusing our attention on the complex exponential of Eq. (3), key factor for the precise localization of targets in radar signals.

2.04.4 SAR Interferometry

In the previous section, we have seen how radar signals allow retrieving the azimuth position of targets with high precision: we just need to exploit the phase of the complex exponential that constitutes the radar system impulse response (see Eq. 3). Such a phase is not meaningful in an absolute way. In fact, the phase is ambiguous, and thus it cannot be used to estimate the target range R_0. However, we can successfully use the phase to estimate range variations. Thus, if the sensor moves, we can estimate $R_0(x)$, the evolution of the target range along the platform moving path. The SAR technology uses this idea to synthesize a big antenna and localize precisely a target in azimuth.

In the previous section, we have also seen that 2D SAR images contain too little information for precisely geolocating SAR targets: we are still missing the third dimension, the height of the analyzed target. In this section, we are going to see how to extract such information from SAR signals. The core idea is again to retrieve it from the phase of the complex exponential in Eq. (3). The way to do it, is again estimating a differential variation of the phase. This time, we are going to exploit two images, acquired at different times, from slightly different satellite positions. This technology is called SAR Interferometry (InSAR). As we will see, the interferometric phase changes according to the ground elevation, leading use to an InSAR-based estimation of the topography.

2.04.4.1 InSAR Geometric Statement

In order to tackle this subject, we assume to deal with two SAR images acquired from two different parallel trajectories. **Fig. 8** sketches the situation: a right-looking platform moves along the same nominal orbit twice and it illuminates the same area on the ground. The reference orbit will be called Master and the other one Slave. The orbits are nominally the same but practically the satellite will be in a slightly different position while taking the second image. As a consequence, a same point on the ground will be observed with a slightly different looking angle in the two acquisitions. We can measure this difference by calculating the distance between Master and Slave positions along the direction orthogonal to the sensor Line of Sight, and we call it Normal (or Interferometric) baseline B_n.

Since the sensor looking angle is slightly different, ground features will be projected onto a slightly different radar geometry. As a consequence, in order to compare the two images and to analyze geometric changes, we need to resample them on a same common grid. Taking the Master image as a reference we can thus resample the Slave one after estimating relative geometric distortions.

Once images are resampled on the same grid, we can focus our attention on geometric changes of the phase of the complex term in Eq. (3). We do this by generating an interferogram, defined as the product pixel by pixel of the Master image times the complex conjugate of the Slave image

$$Int = im_M im_S{}^* = |im_M||im_S|e^{j(\phi_M - \phi_S)}$$

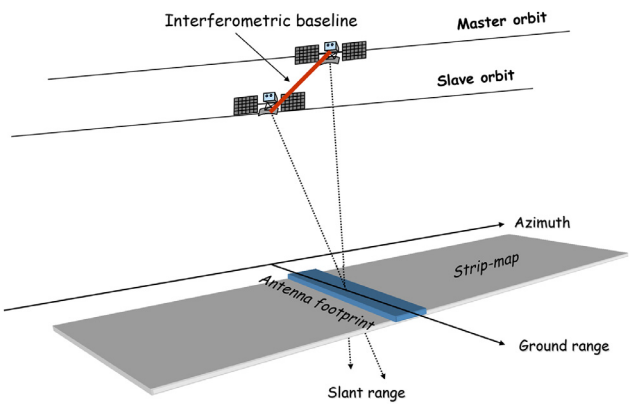

Fig. 8 Sketch of the acquisition geometry of a pair of interferometric SAR images.

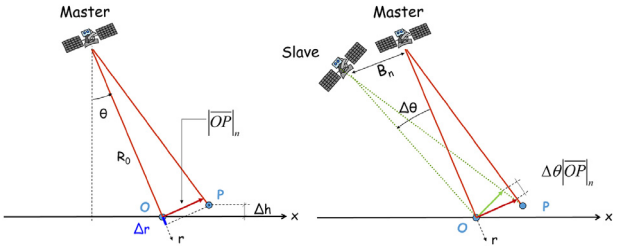

Fig. 9 Interferometric geometry, range section. *Left*: Master acquisition and points P,O. *Right*: Master and Slave acquisitions. Angles in this representation are exaggerated, in reality they are very small and range lines are almost parallel.

The interferometric phase is the difference between the phase of the two images under study (an example of and interferogram is visible in **Fig. 10**). Since the phase is proportional to the range (as seen from Eq. 3), the interferometric phase is a measure of the range change. To quantify the range change, we can refer to **Fig. 9**.

In **Fig. 9**, we see a section of the geometry which contains the range coordinate. We are not going to consider the azimuth one (constant in the picture) because of no interest for this discussion. On the ground we have our target of interest P. For the sake of analyzing the phase of point P, we need to take also a second target O as a reference. The two points are located at a relative height difference Δh and their distance along the range direction is Δr. The sensor observes the two targets from two positions (Master and Slave) and it records four responses in the form of Eq. (3). The relative interferometric phase is obtained as the double difference between points P and O and between images Master and Slave

$$\Delta\phi_{P,O}^{M,S} = \left[\phi^M(P) - \phi^M(O)\right] - \left[\phi^S(P) - \phi^S(O)\right] = \frac{4\pi}{\lambda}\left[R^M(P) - R^M(O) - R^S(P) + R^S(O)\right] \tag{20}$$

Assuming a small Normal Baseline in comparison with the range, all geometric angles in our problem can be considered small, and with simple trigonometry we can easily derive the following expression

$$\Delta\phi_{P,O}^{M,S} = \frac{4\pi}{\lambda}\frac{B_n}{R_0}|OP|_n \tag{21}$$

where $|OP|_n$ is the distance between points P and O along the direction orthogonal to the range.

Eq. (18) states that the interferometric phase between two points is proportional to the distance between them (along the direction orthogonal to the range), and the longer is the Normal Baseline, the higher is the proportionality coefficient. The distance $|OP|_n$ can be projected into slant range Δr and vertical (height) Δh directions (**Fig. 9** on the left).

$$\Delta\phi_{P,O}^{M,S} = \frac{4\pi}{\lambda}\frac{B_n}{R}\frac{\Delta r}{\tan\theta} + \frac{4\pi}{\lambda}\frac{B_n}{R}\frac{\Delta h}{\sin\theta} \tag{22}$$

The first term in Eq. (22) (called "flat terrain") is easily calculated from the orbital information and it can be removed, since it is not carrying any useful information. (**Fig. 10** shows an example of an interferogram before and after removing the flat terrain.) The second term in the equation is directly connected to the objective of our search, the height. We can thus conclude that SAR can be potentially used to estimate the ground topography, and that the way to follow is using Interferometric image pairs.

2.04.4.2 InSAR Challenges

The second term in Eq. (22) shows that the height difference between two targets Δh is directly proportional to the interferometric phase $\Delta\phi_{P,O}^{M,S}$. However, in order to retrieve the topography from an interferometric map, several issues need to be solved.

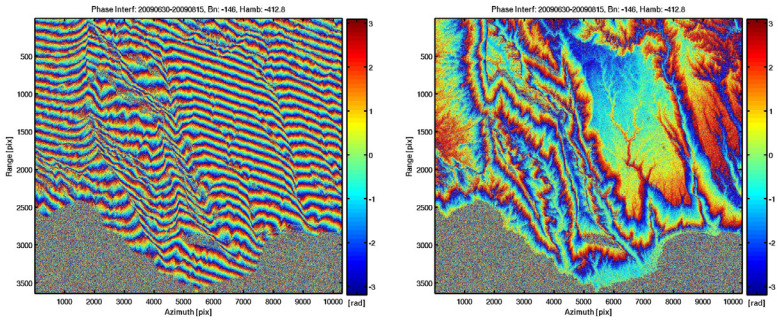

Fig. 10 Example of interferogram before (*left*) and after (*right*) removing the flat terrain. In the *right* image, topographic fringes become more evident.

2.04.4.2.1 Decorrelation

The interferometric phase analyzed above has been derived under the assumption that it is only dependent on the problem geometry. However, the phase of a signal back-scattered by a target may change also because the target itself changes. Any modification of the scattering properties of targets or terrain may in fact lead to a different phase, preventing the correct estimation of the geometric component of the phase. Whenever this happens, the interferogram becomes noisy and we speak of decorrelation of the phase (examples in Fig. 11) (Zebker and Villasenor, 1992). The decorrelation can be measured via the absolute value of the normalized cross-correlation coefficient between Master and Slave images I_M and I_S. We call this index Spatial Coherence γ

$$\gamma = \frac{E[I_M I_S{}^*]}{\sqrt{E[|I_M|^2]E[|I_S|^2]}} \tag{23}$$

When the scattering properties of objects change because of some process evolving in time, we talk of temporal decorrelation. Interferograms with short temporal baseline (time lag between Master and Slave acquisitions) have less probability to be affected by temporal decorrelation. When the cause of the changes is the looking angle (distributed terrain made of many elementary scatterers looks different under different viewing angles) we name it geometric decorrelation. The geometric decorrelation is proportional to the normal baseline, making it more desirable to have short normal baselines to get good coherence. Unfortunately, as it is evident from Eq. (22), a short normal baseline would decrease the phase sensitivity to height, leading to a lower precision in height estimation.

A precondition for estimating the topography through interferometry is high interferometric coherence. In the presence of decorrelation, the geometric phase becomes unreadable (as it can be seen in Fig. 11 on the right).

2.04.4.2.2 Phase unwrapping

Assuming the interferogram is coherent and the phase is readable, to estimate the height from the phase we need to solve phase ambiguities (Goldstein et al., 1988). The phase is in fact wrapped between $-\pi$, π radians. The operation that solves for phase jumps and leads us to a continuous function—whenever possible—is called phase unwrapping. The phase unwrapping operation corresponds to finding a set of integer k multiples of 2π (phase replicas) that connect the wrapped phase ϕ_w to ϕ_{uw}, the continuous jumps-free unwrapped one

$$\phi_{uw} = \phi_w + 2k\pi \tag{24}$$

The concept of phase unwrapping is not difficult; however, implementing it successfully can be very challenging. If the interferometric coherence is not high enough, phase unwrapping can be an impossible task. In Fig. 12, we see an example of interferometric

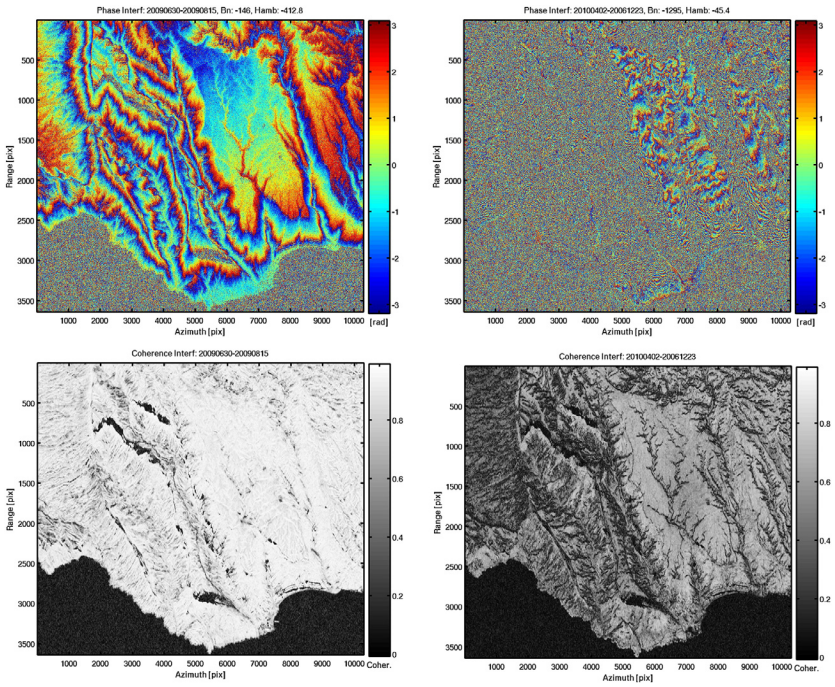

Fig. 11 Two examples of interferograms (*upper line*) and corresponding coherence maps (*lower line*) with different temporal and normal baselines. In the interferogram on the *left*, normal and temporal baselines are small (45 days and 146 m): the phase is clean and the corresponding coherence is high. On the *right*, the images are taken 3 years and 4 months apart and the spatial separation is almost 1300 m: the phase is noisier and the corresponding coherence is lower.

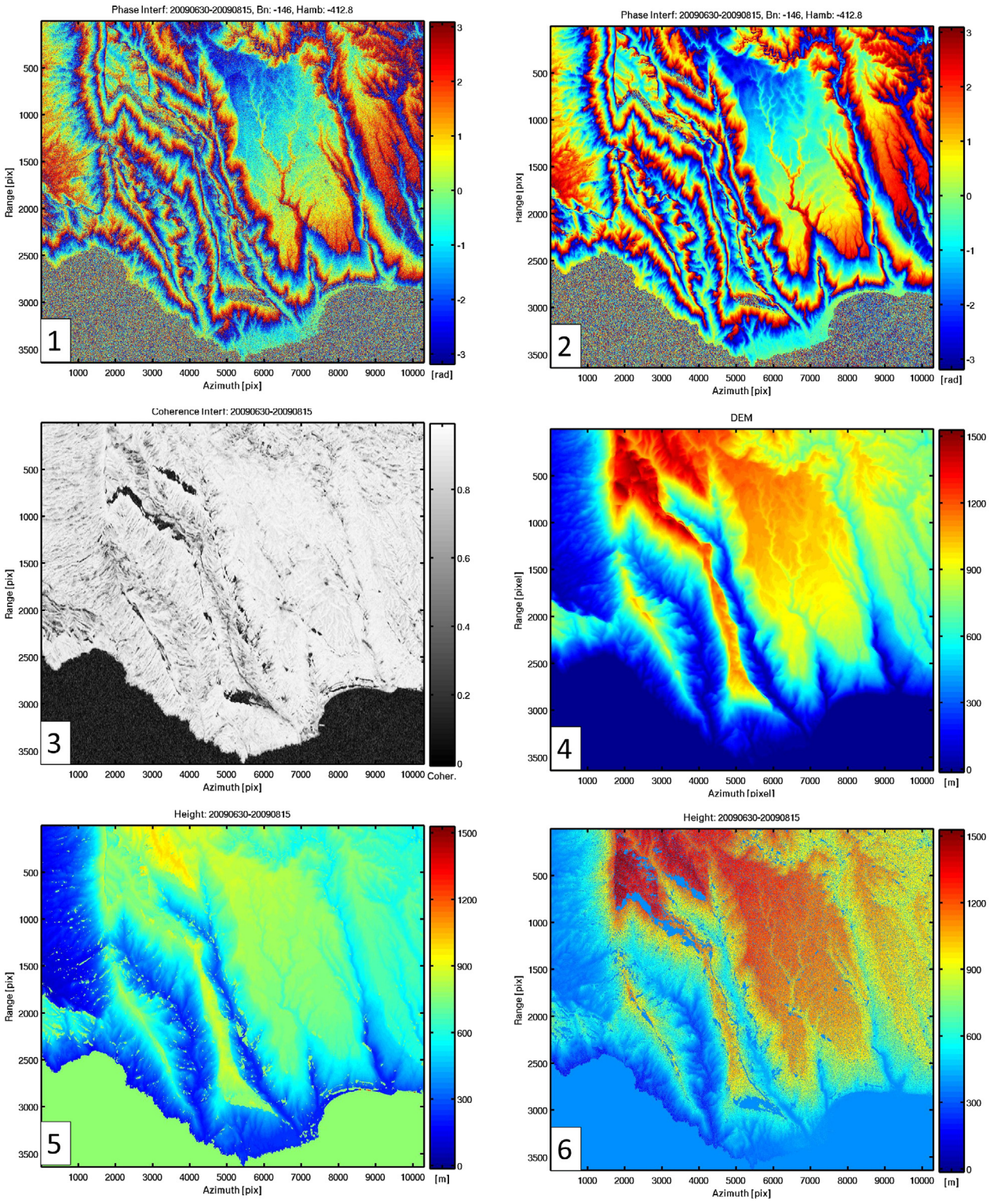

Fig. 12 Interferometric processing example using ALOS data along a mountainous coastline. (A) unfiltered interferogram. (B) filtered interferogram. (C) interferometric coherence. (D) external DEM resampled on the SAR coordinates grid. (E) Unwrapped interferogram where it is evident to see unwrapping errors. The phase has been converted into height for easy comparison with the reference DEM. (F) interferogram unwrapped with a different method. Unwrapping errors are reduced; however, it is evident to see a discrepancy between the result and the DEM. The discrepancy is caused by atmospheric delay.

processing and image 5 is the result of phase unwrapping. The unwrapped phase should match the DEM of the area (Fig. 12 image 4); however, several discrepancies can be noticed. For instance, the peak of the mountain (above 1400 m) in red in image 4 is yellow in image 5: the phase was not unwrapped correctly.

2.04.4.2.3 Ground movements and atmospheric delay

Even by placing ourselves in the best situation, with the highest possible interferometric coherence and easy conditions for successfully unwrapping the phase, the result of our efforts may not be sufficient for retrieving an accurate estimation of the terrain height. In fact, the interferometric phase is a function not only of the acquisition geometry and of the possibly changing scattering mechanism. The interferometric phase may also be affected by ground movements and by the delay caused by atmospheric conditions.

$$\Delta\phi_{P,O}^{M,S} = \Delta\phi_{height} + \Delta\phi_{movement} + \Delta\phi_{atmosphere} \tag{25}$$

The water vapor content in fact, as well as polarized particles, can slow down radar signals traveling through the atmosphere (Hanssen, 2001). Ground movements may be limited by short temporal baselines; however, there is no way to avoid atmospheric delay, unless the two interferometric images are taken simultaneously. A significant amount of research has been conducted in this field, with remarkable contributions. Unfortunately, up to this moment no technology can provide an estimation of the atmospheric delay with similar spatial resolution and sensitivity compared to SAR Interferometry. If the atmospheric delay cannot be precisely estimated and removed, we cannot reliably retrieve the target height. In the next section, we present a solution to separate the different phase components and estimate atmospheric delay when many images are available.

In Fig. 12, image 6 we see the result of an improved algorithm for unwrapping the interferometric phase. This time the estimated height is closer to the one of image 4 (the reference DEM). However, they are not exactly the same: this is an example of phase biased by the atmospheric delay in the area.

2.04.5 Multi-baseline InSAR Positioning

In the previous section, we have seen that SAR has the potential to provide an estimation of the terrain height through interferometry, leading to an independent geolocalization of targets on the Earth Surface. Unfortunately, there are technical issues that prevent from successfully carrying out the job: the interferometric phase may be unreadable, problems may arise in correctly unwrapping the phase, the phase may change because of ground movements and even when those challenges are solved, atmospheric delay may bias the estimation making it unreliable.

In this section, we introduce a technology that can significantly improve the performances of height estimation. The technology is based on the utilization of multiple slightly different viewing angles (multiple interferometric images), the modeling of the different components of the phase, and the joint estimation of the unknowns. Even though many implementations are possible, we are going to tackle the subject in a generic way, and we will call it for simplicity MBInSAR processing (Perissin, 2016).

2.04.5.1 Local MBInSAR

The solution for separating the different components of the interferometric phase starts from the observation that the atmospheric delay changes slowly as a function of the space coordinates. This means that, by analyzing a limited area in space (a few hundred meters in C band), and by choosing a local reference point, the atmospheric delay can be considered small enough to be neglected (left in Fig. 13). The remaining phase components can be modeled as a function of the acquisition parameters and of the target variables. The movement, if any, is expected to be correlated with the acquisition time, and in first approximation it can be considered linear. The topographic component of the phase, as discussed in the previous section, is proportional to the geometric baseline. We can thus write

$$\Delta\phi_{P,O}^{M,Si} \cong \frac{4\pi}{\lambda}\frac{B_{n,i}}{R}\frac{\Delta h_p}{\sin\theta} + \frac{4\pi}{\lambda}B_{t,i}\Delta v_p \tag{26}$$

In Eq. (26), the interferometric phase (between Master and the ith slave image) of point P with respect to a close point O taken as reference, is a function of normal and temporal baselines ($B_{n,i}$ and $B_{t,i}$, respectively). In Eq. (26), we have neglected the first term visible in Eq. (22) (the "flat terrain"), because it can be easily estimated and removed. There are two unknowns in Eq. (26), height Δh_p and velocity Δv_p of point P with respect to reference point O. The atmospheric delay does not appear in 26 because it is assumed small between two close points.

Our aim is estimating the height Δh_p; however, in the presence of possible ground movement, we have to jointly estimate it together with the velocity Δv_p. The problem looks linear, but the observations are taken from a phase and the phase is wrapped. A possible solution comes from an analysis in the complex domain (Ferretti et al., 2001). We can build an objective function γ in dependence of the parameters that we need to estimate, that measures the angular distance between the observed phase $\Delta\phi_{obs}$ and the model in Eq. (26) exploiting N interferometric pairs

$$\gamma(\Delta h_p, \Delta v_p) = \frac{1}{N}\sum_{i=1}^{N} e^{j\left(\Delta\phi_{obs} - \frac{4\pi}{\lambda}\frac{B_{n,i}}{R}\frac{\Delta h_p}{\sin\theta} - \frac{4\pi}{\lambda}B_{t,i}\Delta v_p\right)} \tag{27}$$

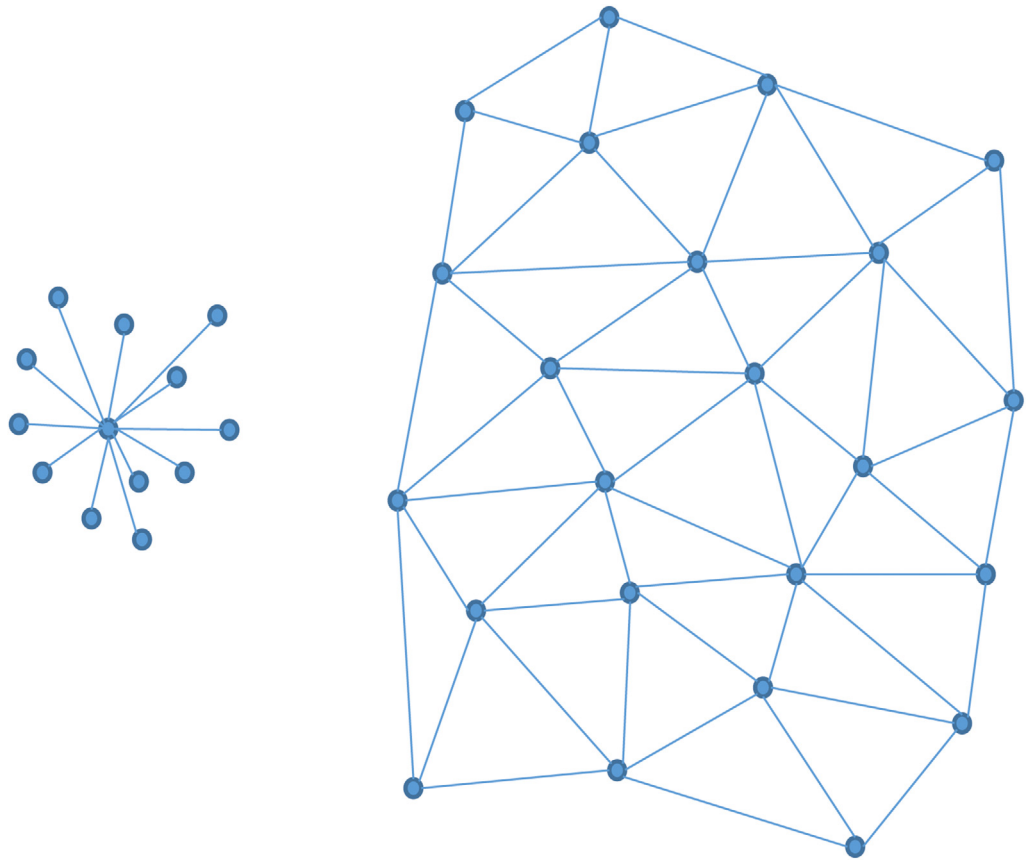

Fig. 13 Local (*left*) and regional (*right*) InSAR configuration schemes. In a small area (*left*) –less than 1 sq km targets can be analyzed with respect to a single reference point, because the atmospheric delay can be assumed small. When bigger areas are processed, a triangulation must be generated in order to keep the atmospheric delay small and still be able to estimate height difference between close points.

Eq. (27) corresponds to a periodogram, where the frequencies to estimate are height and velocity (Ferretti et al., 2007). The solution is found by maximizing the absolute value of γ as a function of height and velocity

$$\left(\Delta\widetilde{h}_p, \Delta\widetilde{v}_p\right) = \arg\max\left\{\left|\gamma\left(\Delta h_p, \Delta v_p\right)\right|\right\} \tag{28}$$

The value of the objective function in the solution gives us a measure of the phase residuals and thus of the reliability of the estimate and it is called Temporal Coherence $\widetilde{\gamma}$

$$\widetilde{\gamma} = \left|\gamma\left(\Delta\widetilde{h}_p, \Delta\widetilde{v}_p\right)\right| \tag{29}$$

We can at this point derive the variance of the estimated height as (Ferretti et al., 2001; Perissin and Rocca, 2006)

$$\sigma^2_{\Delta h} = \left(\frac{\lambda R \sin\theta}{4\pi}\right)^2 \frac{\sigma^2_{\Delta\phi}}{N\sigma^2_{B_n}} \tag{30}$$

Eq. (30) states that the height of a target is estimated with a precision inversely proportional to the number of interferometric pairs and to the dispersion of normal baselines. By substituting numbers of a spaceborne C band sensor as ERS, we can easily reach half a meter standard deviation. We have in this way demonstrated that the radar technology, originally a mono-dimensional system, can in fact be used to localize targets in 3D, thanks to the often-neglected complex exponential of Eq. (3).

2.04.5.2 Regional MBInSAR

MBInSAR can lead us to the precise estimation of the height difference between two close points. This is possible thanks to the assumption that the atmospheric delay between the two points is small enough to be neglected. The outcome of the analysis is remarkable; however, we need to extend the analysis to larger areas if we want it to be practically useful.

The solution can be implemented by adopting a technique similar to triangulation in surveying. We build a redundant network that connects close points (Fig. 13 on the right). We estimate height differences for each connection. Finally, we integrate the height

differences along the graph to retrieve the height of the graph nodes. In formulas we can state the problem using the incidence matrix G, a vector of height differences Δh and a vector of points height h. The direct problem becomes then

$$\Delta h = Gh \tag{31}$$

and the solution of the inverse problem can be found through a least squares inversion

$$h = G^T \left(G^T G\right)^{-1} \Delta h \tag{32}$$

For a successful inversion of the triangulation, the spatial graph needs to be connected (there cannot be interruptions in the graph). This means that all points (targets) selected in the scene need to be coherently connected and must lead to a successful estimation of height differences. The solution of Eq. (32) can be improved by exploiting the temporal coherence in Eq. (29) as a weight.

The successful solution of the spatial triangulation leads us to the estimation of the height of radar targets. This result, together with the estimation of their range and azimuth coordinates, completes the radar 3D localization capability. Eqs. (17)–(19) can thus be solved independently from external data, and the 3D geographic coordinates of targets are estimated.

2.04.6 3D Localization Validation

In the previous sections, we have discussed how radar alone can lead to the estimation of target coordinates in 3D. The key to reach this outcome is the exploitation of multiple radar acquisitions from different viewpoints (firstly to generate images via SAR and then to retrieve the height perspective via InSAR). In literature, the interested reader can find a wide range of demonstrations of the localization capability of this technology (Perissin, 2008). However, as a matter of fact, an extensive statistical validation has never been carried out. Target coordinates have been estimated and cross-validated for small sets of corner reflectors by different authors (Dheenathayalan et al., 2016), but never for a big number of randomly detected radar targets. Here we want to conclude this review by bringing an indirect validation. The analysis proposed here is not based on ground truth validation but on a statistical analysis of the estimated coefficients. The following results do not prove the accuracy of the technology, but they give a demonstration of its precision. In any case, it is useful to stress that the radar 3D localization capability is possible, thanks to the phase of the radar signal. And the phase can be analyzed only in a differential form. As a consequence, the 3D results are relative, and an external ground reference is required to correct for 3D biases.

The statistical validation we want to propose here is based on the analysis of stripmap SAR images taken by the Cosmo SkyMed sensor over different test sites. Fig. 14 shows the orthorectified reflectivity map of a Cosmo dataset taken over Hong Kong, displayed

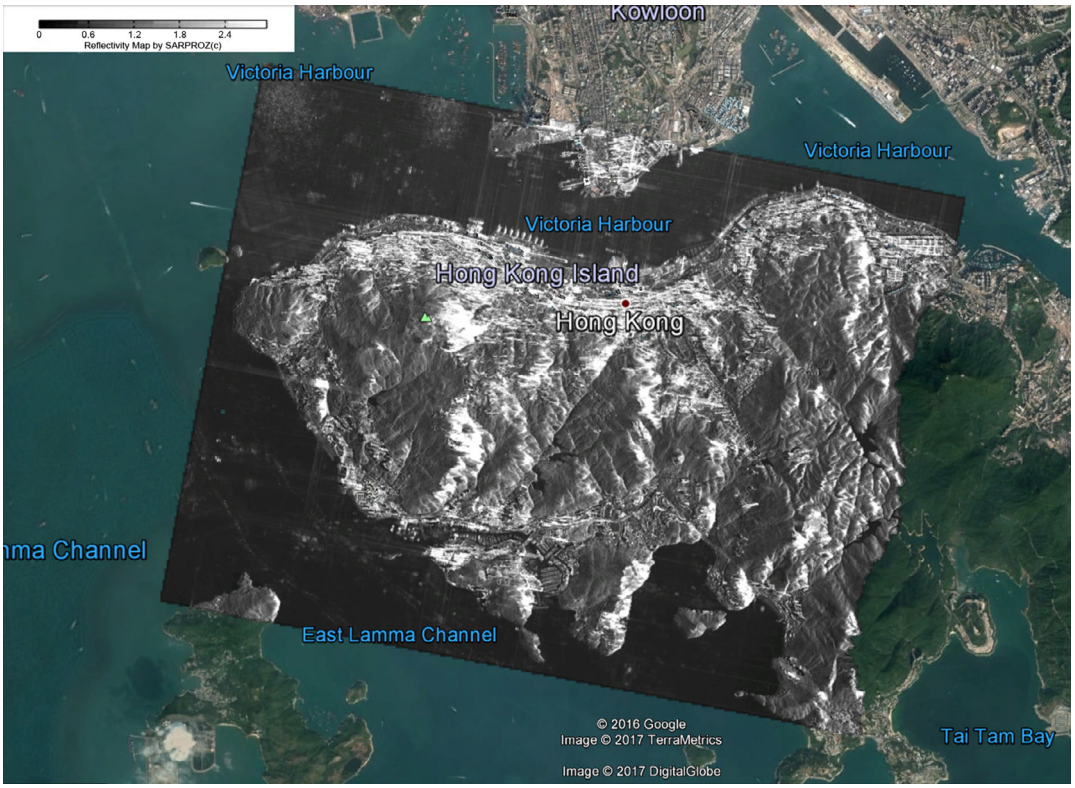

Fig. 14 Orthorectified SAR reflectivity map over the Hong Kong Island. Cosmo SkyMed data.

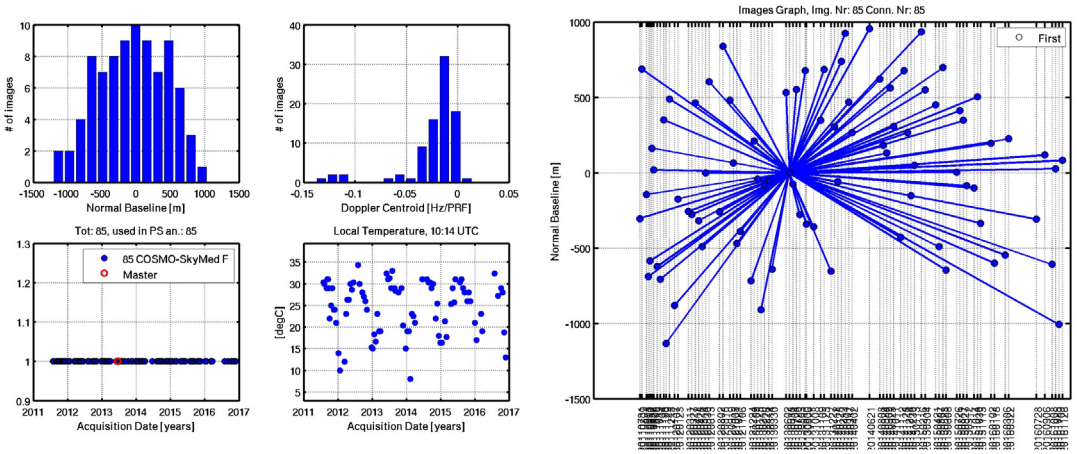

Fig. 15 Cosmo SkyMed dataset used for the validation. The 85 images have been acquired between mid-2011 and the end of 2016. On the *left* in clockwise order, starting from the *upper left* corner: histogram of Normal Baselines, histogram of Doppler Centroids, temperature time series, time distribution of the images. *Right*: each dot represents an image in the normal baseline/time domain. All images are connected to the reference Master image (acquired on June 18, 2013).

in Google Earth. Fig. 15 reports the geometric distribution of the corresponding images. In all data samples, pixel spacing is about 2 by 2 m (range and azimuth) on the ground (images are taken in stripmap mode). The Hong Kong processed area is about 5000 by 4000 pixels, around 20sqkm.

Data have been processed with the software Sarproz developed by the author (Perissin et al., 2011). The interested reader can apply for a license of the software to reproduce the results shown here.

All images need to be firstly coregistered on the same grid of the master image. The statistics of the coregistration process represent the first outcome of our validation. In fact, they give us an idea of the relative dispersion of SAR coordinates. In Fig. 16, we see the result of 280 Cosmo Skymed images. Fig. 16 has been generated computing the histograms of the estimated azimuth (top row) and range (bottom row) shifts (left columns) and stretches (right column). Shifts and stretches have been estimated by amplitude cross-correlation of image patches, and they have been corrected for geometric distortions predicted from orbital data. As previously

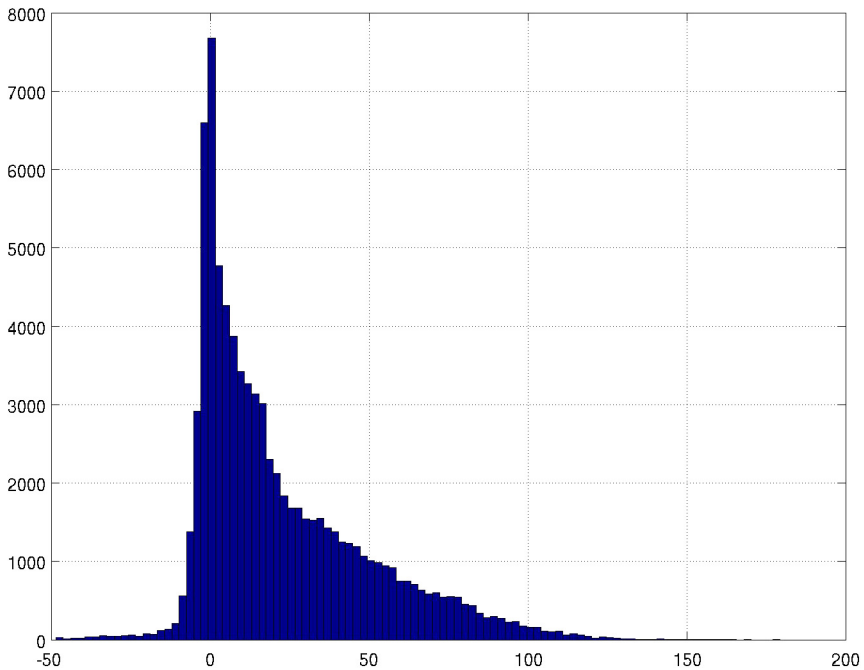

Fig. 16 Coregistration statistics: *upper row*, Azimuth Offset (*left*) and stretch (*right*); *lower row*: Range Offset (*left*) and stretch (*right*). An outlier with about 50 lines azimuth offset and 500 samples range offset was removed.

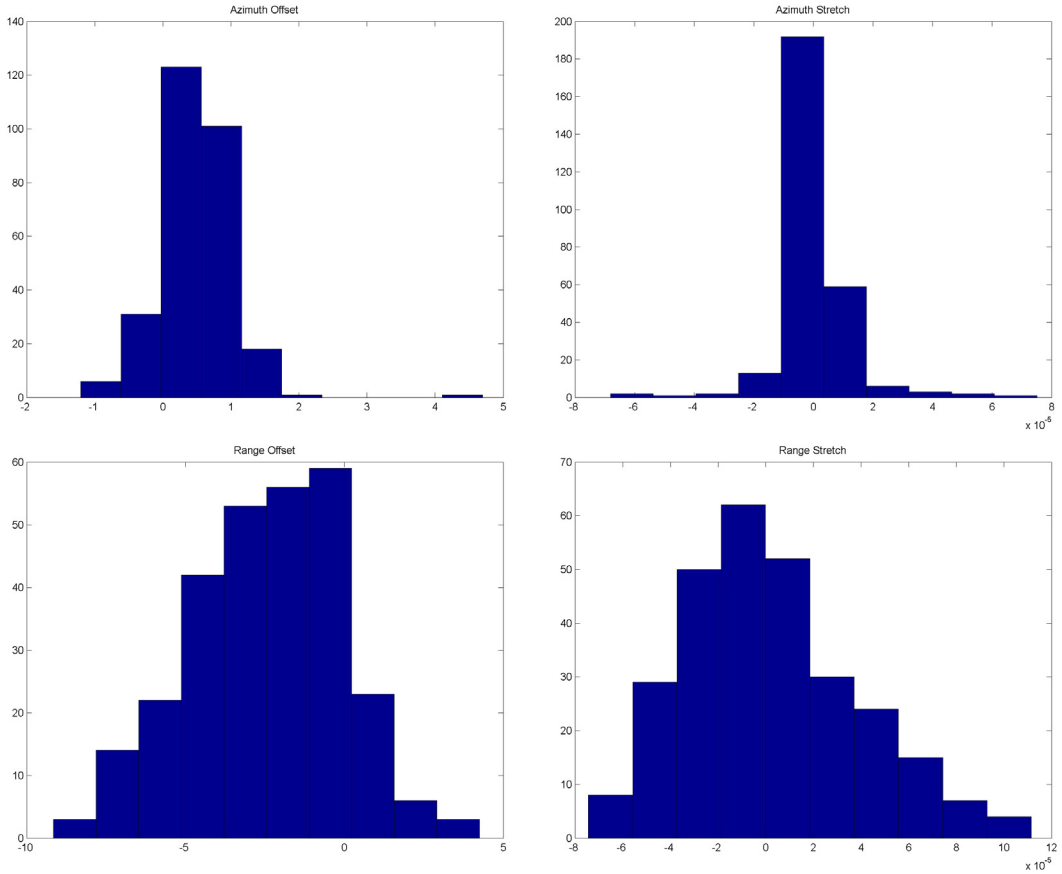

Fig. 17 Histogram of the estimated height of SAR targets in Hong Kong.

mentioned, we can see that orbital information is fairly precise: stretch coefficients dispersion is in the order of 10^{-5} (less than a 10th of pixel over the whole analyzed area). However, standard deviations of range and azimuth offsets are in the order of few pixels (being the azimuth coordinate more precise than the range one). Moreover, the histograms clearly show a bias with respect to zero, meaning that the selected master image was probably itself misplaced. In other words, as stated in previous sections, orbital trajectory coefficients are precise to fractions of meters, but orbital offsets (timing and range of the first pixel) are affected by higher uncertainty. This issue leads to possible rigid mislocation of SAR targets. (Sarproz provides several means to estimate and correct such shifts.)

As discussed in previous sections, we need a third condition to geolocate targets: the height. The procedure for estimating it has been previously described: we exploit a multibaseline dataset to estimate height differences from close targets. We repeat the analysis over a triangulation network and we retrieve the height of all analyzed targets in the region of interest. We have carried out the estimation for the Hong Kong test site and we processed about 80,000 targets. We provide here again an indirect validation: Fig. 17 shows the histogram of the estimated height after removing a high-resolution external Digital Terrain Model (DTM) of Hong Kong. The histogram reveals that most of targets are over the terrain level (as reasonably expected, since signals do not penetrate the ground). But the most interesting outcome is actually the histogram peak at zero elevation. The peak reveals in fact targets located at terrain level. The high concentration of targets at ground level allows us to retrieve a quantification of the dispersion of the height estimate that can be assessed in slightly more than 1 m in this dataset. The peak shown here is precisely centered at zero, but this is again the outcome of a software correction. Normally, we should expect a bias also in the height domain.

2.04.7 Conclusions

In this article, we reviewed the 3D localization capability of radar signals, with particular emphasis to satellite remote sMensing microwave imaging. We have treated the subject using the phase of radar signals as the key interpreting factor. The phase is in fact sensitive to very small range variations, allowing a 3D geometric reconstruction of objects observed from different viewing angles. We have then concluded the discussion providing some statistics based on real data acquired by SAR sensors (Fig. 18).

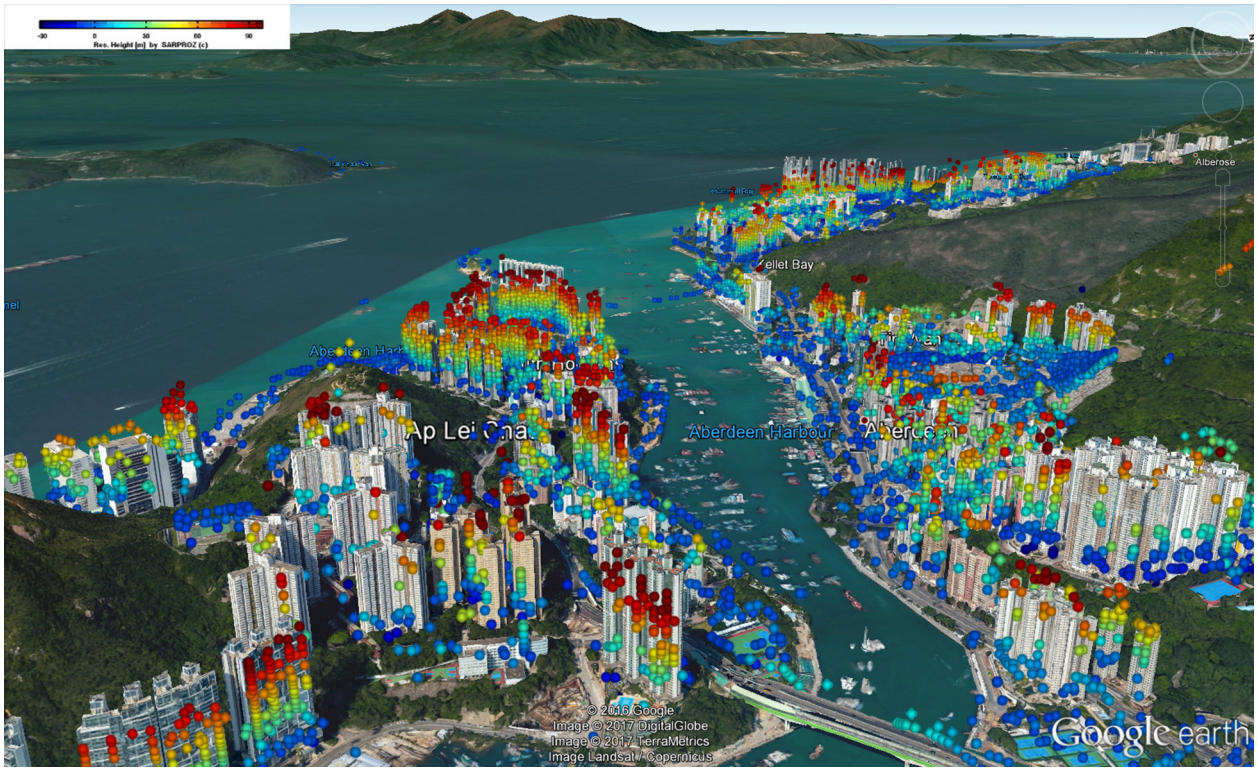

Fig. 18 Final result, showing the geolocalization of radar targets in 3D, displayed in Google Earth together with 3D building models. Each colored dot is a target retrieved from the Cosmo Skymed analyzed dataset. The color is proportional to the estimated height.

See also: 1.16. Microwave Sensors. 1.18. Remote-Sensing Missions and Sensors—Radar Sensors. 2.02. Geometric Processing: Optical Sensor Modeling and Calibration. 2.03. Geometric Processing: Active Sensor Modeling and Calibration (LiDAR).

References

Allan, T. D. (1983). *Satellite microwave remote sensing*. Chichester: Ellis Horwood.
Bamler, R., & Hartl, P. (1998). Synthetic aperture radar interferometry. *Inverse Problems, 14*, R1.
Curlander, J. C., & McDonough, R. N. (1991). *Synthetic aperture radar*. New York: John Wiley & Sons.
Dheenathayalan, P., Small, D., Schubert, A., & Hanssen, R. F. (2016). High-precision positioning of radar scatterers. *Journal of Geodesy, 90*(5), 403–422.
Ferretti, A., Prati, C., & Rocca, F. (2001). Permanent scatterers in SAR interferometry. *IEEE Transactions on Geoscience and Remote Sensing, 39*, 8–20.
Ferretti, A., Monti-Guarnieri, A., Prati, C., Rocca, F., & Massonet, D. (2007). *InSAR principles-guidelines for SAR interferometry processing and interpretation, 19*. Noordwijk: ESA Publications.
Goldstein, R. M., Zebker, H. A., & Werner, C. L. (1988). Satellite radar interferometry: Two-dimensional phase unwrapping. *Radio Science, 23*, 713–720.
Hanssen, R. F. (2001). *Radar interferometry: Data interpretation and error analysis* (vol. 2). London: Springer.
Massonnet, D., & Feigl, K. L. (1998). Radar interferometry and its application to changes in the Earth́s surface. *Reviews of Geophysics, 36*, 441–500.
Perissin, D. (2008). Validation of the submetric accuracy of vertical positioning of PSs in C-band. *IEEE Geoscience and Remote Sensing Letters, 5*, 502–506.
Perissin, D. (2016). Interferometric SAR multitemporal processing: Techniques and applications. In *Multitemporal remote sensing* (pp. 145–176). Berlin, Germany: Springer.
Perissin, D., & Rocca, F. (2006). High-accuracy urban DEM using permanent scatterers. *IEEE Transactions on Geoscience and Remote Sensing, 44*, 3338–3347.
Perissin, D., Wang, Z., & Wang, T. (2011). *The SARPROZ InSAR tool for urban subsidence/manmade structure stability monitoring in China*. In Sidney: Proceedings of the ISRSE, 1015.
Zebker, H. A., & Villasenor, J. (1992). Decorrelation in interferometric radar echoes. *IEEE Transactions on Geoscience and Remote Sensing, 30*, 950–959.

Further Reading

Moreira, J., Schwabisch, M., Fornaro, G., Lanari, R., Bamler, R., Just, D., et al. (1995). X-SAR interferometry: First results. *IEEE Transactions on Geoscience and Remote Sensing, 33*, 950–956.